J Solid State Electrochem (2012) 16:3429–3441
DOI 10.1007/s10008-012-1830-4

ORIGINAL PAPER

Electrodeposition of Ni/ceria composites: an in situ visible reflectance investigation

Hossein Hassannejad · Claudio Mele · Taghi Shahrabi · Benedetto Bozzini

Received: 11 April 2012 / Revised: 17 July 2012 / Accepted: 18 July 2012 / Published online: 1 August 2012

Abstract Ni/cerium oxide coatings were electrodeposited from particle-free aqueous baths containing $NiCl_2.6H_2O$ and $CeCl_3.7H_2O$. The mechanism of deposition was studied systematically by a combination of voltammetric, in situ spectroelectrochemical (visible reflectivity spectroscopy (VRS) and surface Raman spectroscopy), ex situ spectroscopic (spectroscopic ellipsometry) methods, as well as by scanning electron microscope imaging; yielding details on the steps of the composite formation process. Time- and potential-dependent electro VRS data were interpreted on the basis of an optical model, accounting for the formation of metal and ceramic phases and corresponding relative distribution and morphology. In the VRS curves measured with the pure Ni and Ce-containing solutions, the value of reflectivity drops sharply when the potential is lower than ca. −0.9 V. The VRS curves measured in the Ce-containing solutions exhibit a second drop when the potential is lower than ca. −1.1 V while, instead, for pure Ni solution an increase in reflectivity is observed. According to the proposed optical model, the drop found in the reflectivity transient can be explained with the nucleation of Ni on the Cu substrate, while the second one measured with Ce-containing solutions is due to secondary nucleation of Ni. The results showed that the deposition processes of Ni and Ni/cerium oxide can be divided into two and four stages, respectively. (1) In the case on Ni: nucleation and 3D growth, accompanied by roughening; (2) as far as Ni/cerium oxide is concerned: nucleation, formation of cerium oxide, secondary nucleation, and 3D growth and roughening.

Keywords Electrodeposition · Cerium oxide · Ni · Composite · Spectroelectrochemistry · Spectroellipsometry · Visible reflectivity · Raman

H. Hassannejad · C. Mele · B. Bozzini (✉)
Dipartimento di Ingegneria dell'Innovazione,
Università del Salento,
via Monteroni,
73100 Lecce, Italy
e-mail: benedetto.bozzini@unisalento.it

T. Shahrabi
Department of Materials Science and Engineering,
Tarbiat Modares University,
P.O. Box 14115-143, Tehran, Iran

Present Address:
H. Hassannejad
Department of Materials Science and Engineering,
Tarbiat Modares University,
P.O. Box 14115-143, Tehran, Iran

Introduction

Rare earth compounds, and especially cerium oxide, owing to their special physical and chemical characteristics, exhibit a range of outstanding functional properties and have been used successfully in many applications such as: optics, electronics, catalysis, metallurgy, chemical, and materials engineering [1, 2]. Electrochemical synthesis of ceramic materials, especially oxides, has received considerable attention in recent years because of the low cost of equipment and sound thickness control capabilities. There are basically two types of electrochemical methods that have been employed in the synthesis of cerium oxide: cathodic base generation and anodic oxidation [1–7]. Cathodic deposition was used to produce oxides and hydroxides by precipitation in the catholyte induced by the hydroxide produced in the vicinity of the working electrode by water hydrolysis. The electrochemical mechanism of base electrogeneration during cathodic deposition has been widely discussed in the literature [8–13] and can be schematised with the following system of equations:

$$\left.\begin{array}{l} 2H^+ + 2e^- \rightarrow H_2 \\ 2H_2O + 2e^- \rightarrow H_2 + 2OH^- \\ O_2 + 2H_2O + 4e^- \rightarrow 4OH^- \\ O_2 + 2H_2O + 2e^- \rightarrow 2OH^- + H_2O_2 \end{array}\right\} \quad (1)$$

The above reactions generate hydroxide ions thus promoting the formation of a $Ce(OH)_3$ precipitate or of complexes of the form $Ce(OH)_2^{2+}$ or of related oligomers [8–10].

$$\left.\begin{array}{l} Ce^{3+} + 3OH^- \rightarrow Ce(OH)_3 \\ 4Ce^{3+} + O_2 + 4OH^- + 2H_2O \rightarrow 4Ce(OH)_2^{2+} \\ 2Ce^{3+} + 2OH^- + H_2O_2 \rightarrow 2Ce(OH)_2^{2+} \end{array}\right\} \quad (2)$$

Finally, with a further pH increase in the vicinity of the cathode, CeO_2 is formed [8–10]:

$$\left.\begin{array}{l} Ce(OH)_3 \rightarrow CeO_2 + H_3O^+ + e^- \\ Ce(OH)_2^{2+} + 2OH^- \rightarrow CeO_2 + 2H_2O \end{array}\right\} \quad (3)$$

In recent years, Ni and Ni-based alloys containing cerium oxide have raised interest in surface engineering because of their excellent wear, corrosion, and oxidation resistance, accompanied by outstanding mechanical properties [14–16]. Moreover, Ni-based cerium oxide composites have been considered in the literature as potentially interesting catalysts, since they show excellent activity towards methane decomposition [17] and partial oxidation [18], hydrogen evolution [19], and the water–gas shift reaction [20]. Among the different techniques that have been used to produce Ni/cerium oxide composite coatings, co-electrodeposition is one of the simplest and cheapest methods. Since, as recalled above, cerium oxide can be grown by cathodic deposition, a new method has been recently proposed for the fabrication of Ni/cerium oxide coatings by depositing both metal and oxide from the same solution [21]. The authors of this work used electrochemical impedance spectroscopy to characterise the electrodeposition process: even though interesting information was obtained with this approach, only a limited mechanistic understanding was achieved. In fact, an intrinsic drawback of merely electrochemical approaches to the study of Ni/cerium oxide electrodeposition is the simultaneous hydrogen evolution which makes it difficult to single out information on film growth kinetics. Therefore, in this work, we resorted to using spectroelectrochemical methods in order to address more directly the dynamic cathodic interface: these techniques have been demonstrated to offer a wealth of information on electrodeposition processes [13, 22–29]. In particular, the aim of this study was to investigate the Ni/cerium oxide electrodeposition mechanism by concentrating on in situ measurement of visible reflectivity spectroscopy (VRS). For this purpose, reflectivity was measured during the deposition of pure Ni and Ni-matrix composite coatings with low and high cerium oxide contents, respectively denominated "Ni/low-cerium" and "Ni/high-cerium" in the rest of this paper. In order to achieve an insightful understanding of our dynamic in situ reflectivity data, we resorted to ancillary spectroscopic measurements (surface Raman spectroscopy and spectroellipsometry) and to optical modelling of the composite/electrolyte interface.

Experimental

Materials

Reagent grade $NiCl_2.6H_2O$ (0.05 M) and H_3BO_3 (0.5 M) were used to prepare the basic Ni electrodeposition bath. A suitable amount of catholyte buffer (H_3BO_3) is required in order to fine-tune the precipitation of Ce-containg species during the electrodeposition of metallic Ni. The reagents were dissolved in ultrapure water of resistivity >18 MΩ cm, produced with a Millipore Milli-Q system. The pH of the solutions was adjusted by addition of dilute HCl to 3.0± 0.1. It is worth noting that the pH values of cognate baths described in the literature recalled above lie in the range of 2–4. $CeCl_3.7H_2O$ 1 and 5 mM were added to the Ni basic bath to prepare solutions with different cerium ion concentrations. By increasing the $NiCl_2/CeCl_3$ concentration ratio in the range of 0–0.2, an increase in concentration in the

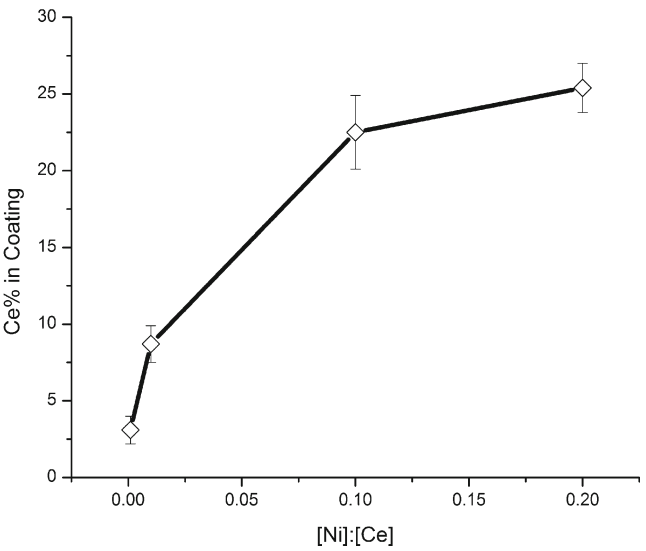

Fig. 1 Dependence of Ce concentration—as measured by EDX—in coating on the $NiCl_2/CeCl_3$ concentration in the bath ($NiCl_2$ 0.05 M, H_3BO_3 0.5 M, pH 3 by HCl electrodeposition at −1.3 V for 30 min)

deposits is obtained, under typical plating conditions (−1.3 V, 30 min), as shown in Fig. 1, reporting energy-dispersive X-ray spectroscopy (EDX) measurements. Our solutions were air saturated, thus O_2 provides the reagent the reactions involved in Eq. (1). H_2O_2 could have been added to the bath formulation to achieve the same result; but on the basis of previous experience, we chose the option of working with the air-saturated bath. It is worth stressing, after the detailed analysis of [10], that with air exposure, the precipitate typically contains Ce(IV) oxide. By saturating the solution with Ar, instead a colourless gel precipitate is obtained, not containing Ce(IV) oxide. Moreover, the presence of O_2 has a major bearing on Ce (III) hydrolysis and precipitation processes. The substrates were polycrystalline Cu (either 100 μm thick foils or discs: the former were used in the as-laminated state, the latter were polished metallographically to mirror finish); the substrates were degreased with acetone and etched with 0.1 M sulphamic acid before electrodeposition. Cu was chose for two chief reasons: (1) our Ni-based coatings exhibit a very good adhesion to Cu, (2) the nature of hydrogen overpotential on Cu makes this cathode well suited for the investigation of the initial stages of electrodeposition of a Ni-based material.

Preparation of calibration samples for spectroellipsometry

The baths described in the "Materials" section were employed to electrodeposit three reference samples, representing limiting cases of Ni/cerium oxide composites: (1) pure Ni, from the basic Ni bath; (2) Ni/low-cerium oxide composite, from the 1 mM $CeCl_3$ bath; and (3) Ni/high-cerium oxide composite, from the 5 mM $CeCl_3$ bath. A potential of −1.5 V vs. Ag/AgCl was applied for deposition of nickel film on a Cu electrode for 600 s.

Spectroscopic ellipsometry measurements and modelling

Spectroscopic ellipsometry (SE) is a technique which provides an accurate estimate of the optical properties of surfaces. SE measurements yield two functions $\Delta(\lambda)$ and $\psi(\lambda)$ of the wavelength λ that are associated with the complex refractive index of the material. These functions depend on material properties of the film/substrate multilayered structure, as well as on film thickness and roughness. Δ and ψ can be modelled with standard optical physics approaches, that are implemented in commercial software, such as Deltapsi II, that we have employed for the present study. Multilayer modelling includes: (1) the sequence of the layers and their respective thicknesses, (2) the complex refractive indices of the materials, (3) effective-medium information (e.g. with the Bruggeman effective medium approximation, available in Deltapsi II), if required for the simulation of disperse films, and (4) a model for roughness. The Deltapsi II software iteratively fits the model to the measured data, minimising the mean square error (MSE) defined as:

$$\mathrm{MSE} = \frac{1}{n-1} \cdot \sum_{i=1}^{n} \left[\left(\psi_i^c - \psi_i^e\right)^2 + \left(\Delta_i^c - \Delta_i^e\right)^2 \right] \qquad (4)$$

where c and e stand for the calculated and experimental data respectively and n is the number of experimental points. Accurate model discrimination work—based on the results of [30, 31]—yielded the system depicted in Fig. 2a as the best one to interpret the three investigated types of films, representing limiting cases of the electrodeposition processes of interest. As customary in multilayer optical modelling, roughness effects are computed by considering a void volume fraction: such geometrical model corresponds to assuming that the optically effective film thickness corresponds to the envelope of the roughness features. Within this framework, the fitting parameters are thus: the film thickness t and the volume fractions f_1 and f_2 for Ni and cerium oxide, respectively. In order to correlate the optical models with experimental data, the void volume fraction $V=1-f_1-f_2$ ought to be interpreted in terms of an appropriate roughness model in order to represent more closely a real physical condition [32, 33]. In this study, we used the sawtooth roughness model depicted in Fig. 2b and derived the parameter a ("arithmetic average of absolute values" AAR estimator) experimentally. Geometrical information was fed into the optical model by defining the void fraction as: $V = \frac{a}{2 \cdot t}$. Of course, owing to the adopted geometrical definition, Deltapsi II allows to estimate roughness effects only for $a \leq t$. In order to use this model to simulate growth from the aqueous phase, an adequate top layer of water has been added as well; from the optical path of the beam in the bath, the thickness of such layer has been set to 1 mm.

Linear sweep voltammetry and in situ electro VRS

Linear sweep voltammetry (LSV) measurements were carried out in a three-electrode system with a scan rate of 10 mV s^{-1}. The working electrode was a polycrystalline Cu disc (diameter, 5 mm), the reference electrode was Ag/AgCl and the counter electrode was a Pt wire. All potentials are reported on the Ag/AgCl scale. The initial and terminal voltages were −0.3 and −1.8 V, respectively. The system used for in situ Electro VRS was built in our laboratory and is described in detail elsewhere [32, 33]. The electrolytes we employed were the three chloride-based

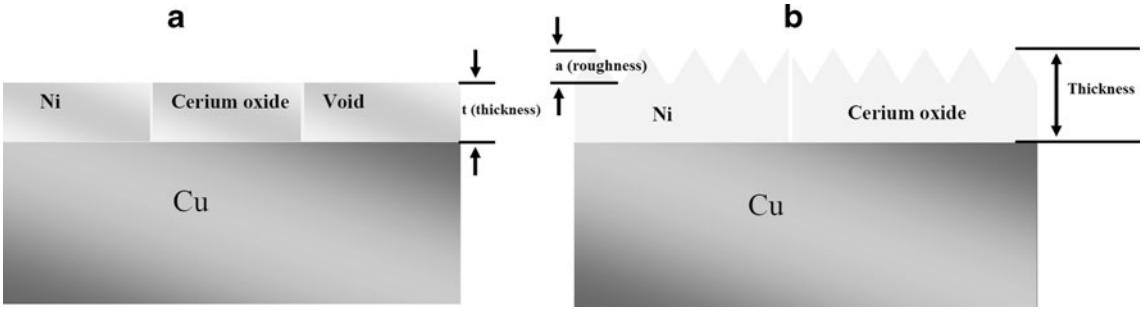

Fig. 2 Optical model of a Ni/cerium oxide composite film on Cu substrate, used for the simulation of reflectivity and spectroscopic ellipsometry data. **a** Classical optical model, accounting for roughness via a void fraction. **b** Corresponding model, interpreting the void fraction in terms of a standard geometrical model

solutions with different cerium ion concentrations, described in the "Materials" section.

Characterisation of the films

In order to achieve a better understanding of the relationship between growth morphology and optical properties, three samples were prepared by stopping the linear potential sweep at different end potentials: −1.0, −1.3, and −1.8 V, corresponding to critical points of both reflectivity and current density transients (see "In situ visible reflectivity spectroscopy" section for details). The surface of the coatings was studied with scanning electron microscope (SEM, Jeol JSM 6480-LV) and, in the case of thicker coatings, their composition was assessed by EDX (SphinX 130 IXRF), semiquantitative compositional data were estimated with a ZAF correction method. An Alpha Step 500 Surface Profiler was also used to measure roughness and thickness of these coatings. The chemical state of Ce in the film was determined by X-ray photoelectron spectroscopy (XPS). The XPS analysis was carried out on a PHI-5700 ESCA system using an Al Ka (1,486.6 eV) X-ray source. The surface was cleaned using 1 min of Ar^+ etching before analysis.

Surface Raman spectroscopy

Surface Raman spectroscopy measurements were performed with a Raman microprobe system (LabRam Jobin-Yvon) equipped with a confocal microscope, CCD detector, holographic notch filter, and mapping facilities with micrometric lateral resolution. The excitation line was 632.8 nm from an HeNe laser delivered at the sample point with about 12 mW. A 50× long-working distance objective was used. In situ electrochemical measurements were carried out in a Ventacon cell with a vertical polycrystalline Cu disc working electrode of 5 mm diameter embedded into a teflon holder.

Results and discussion

Model selection based on spectro-ellipsometry

The experimental and fitted $\Delta(\lambda)$ and $\psi(\lambda)$ curves for Ni, Ni/low-cerium oxide and Ni/high-cerium oxide films electrodeposited by LSV are presented in Fig. 3. In order to achieve reliable nonlinear least-squares fitting results, we used the approach proposed in [34, 35]. The good matching of the experimental and computed curves proves the accuracy of the selected model.

In situ visible reflectivity spectroscopy

Figure 4 shows the in situ VRS measurements obtained during electrodeposition from the three different solutions described in the "Materials" section onto the Cu electrode. In all the curves, it can be observed that the reflectivity value drops sharply when the potential is lower than ca. −0.9 V. The reflectivity curves measured in the Ce-containing solutions exhibit a second reflectivity decrease interval when the potential is more cathodic than ca. −1.1 V, while, instead, for the pure Ni solution only an increase in reflectivity is observed. In the following "Reflectivity transient recorded during nickel electrodeposition" and "Reflectivity transient recorded during electrodeposition from the Ni/high-cerium solution" sections, we shall discuss separately the reflectivity curves recorded with the three different electrodeposition baths.

Reflectivity transient recorded during nickel electrodeposition

The LSV and VRS curves measured with the pure Ni solution are shown in Fig. 4a. The reflectivity curve can be divided into three regions. In region I, upon decreasing the

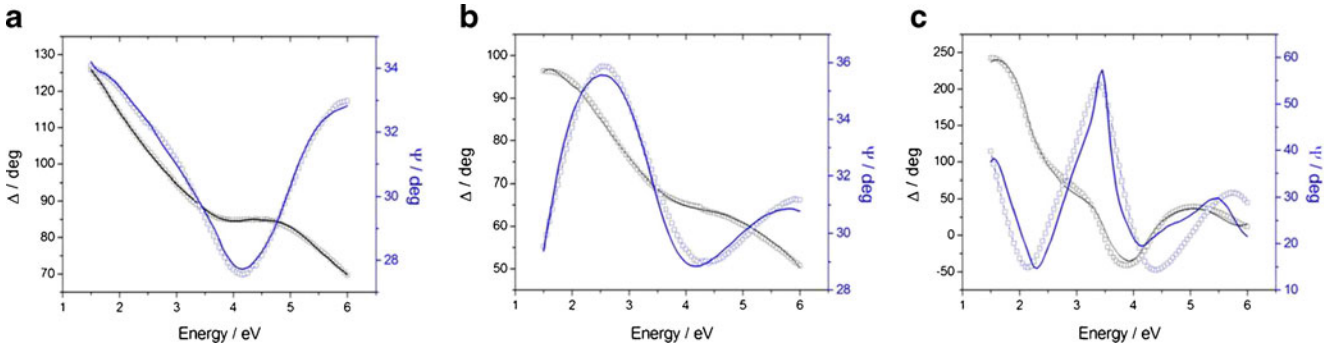

Fig. 3 Experimental (*scatter plot*) and fitted (*continuous lines*) spectroellipsometric $\Delta(\lambda)$ and $\psi(\lambda)$ curves for electrodeposited: **a** Ni, **b** Ni/low-cerium oxide, and **c** Ni/high-cerium oxide films

potential from −0.3 to −0.9 V, the value of reflectivity is approximately constant. The LSV curve also shows that the value of current density is ca. zero in this range, showing that in this region there is no reaction. In region II, a further decrease in the potential value from −0.9 V causes a drop in the reflectivity. By decreasing the potential value below −1.1 V, the reflectivity starts to increase and at the end of region II (i.e at ca. −1.45 V), a maximum is attained. Reducing the voltage to still lower values, in region III, the reflectivity exhibits a steady decrease.

Since from the literature [34], it is known that hydrogen evolution does not measurably affect the value of reflectivity, this decrease can be related to the nucleation of Ni. In order to substantiate our interpretation of changes in reflectivity, we used the optical model illustrated in the "Model selection based on spectro-ellipsometry" section, selecting appropriate parameter values for the different stages of growth of the Ni film. Figure 5a illustrates the simple model we propose to follow the process of Ni nucleation. As anticipated in "Spectroscopic ellipsometry measurements and modelling" section—on the basis of fitting work with the three-materials model described above—in the simulation of nucleation we adopted the Maxwell–Garnett (MG) approach, which describes the optical properties of a composite, consisting of nanosized inclusions embedded in a given host material [32]. We assume that the equivalent optical thickness of the MG material, corresponding to a monolayer of hemispherical nuclei generated by an instantaneous nucleation act, equals the radius of the hemispherical nuclei themselves. Assuming that a hexagonal compact array of nuclei forms on the cathode, the radius of the collided nuclei can be approximated as half the distance between two such Ni nuclei. Of course, this assumption is a very crude one and only captures some integral features of the effects of surface coverage with electrodeposted nuclei. Nevertheless it is seems adequate for the exploratory modelling necessary for the rationalisation of the original approach proposed in this work. Moreover, the sensitivity of the model outcomes to the arrangement of nuclei is very limited. Figure 5b illustrates the simple geometrical model used to calculate this distance. The following relation was used to estimate the distance a between two Ni particles:

$$a = \sqrt{\frac{2}{\sqrt{3} \cdot N_0}} \tag{5}$$

where N_0 is the number density of Ni nuclei in the indicated arrangement. In the literature, typical N_0 values reported for

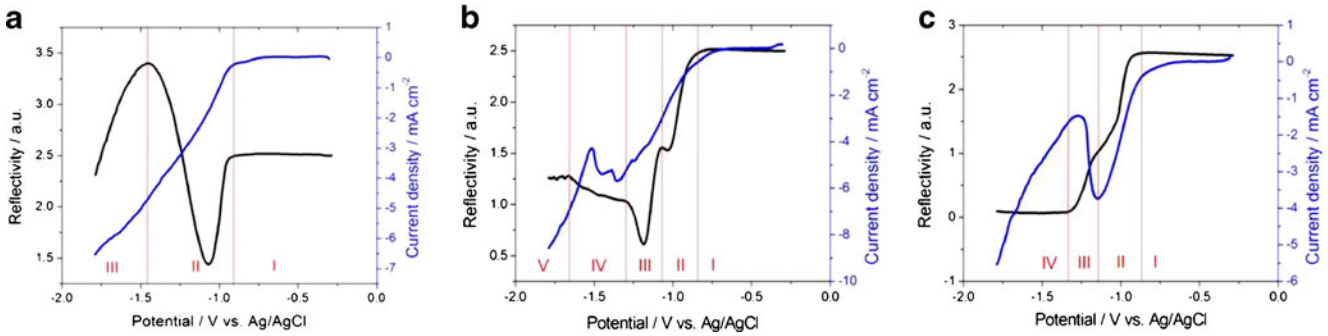

Fig. 4 In situ VRS measurements at 400 nm during LSV for a Cu electrode in contact with **a** Ni, **b** Ni/low-cerium, and (**c**) Ni/high-cerium solutions. The potential is swept from −0.3 to 1.8 V with a sweep rate of 10 mV s^{-1}. *Black lines* reflectivity curves; *blue lines* current density curves

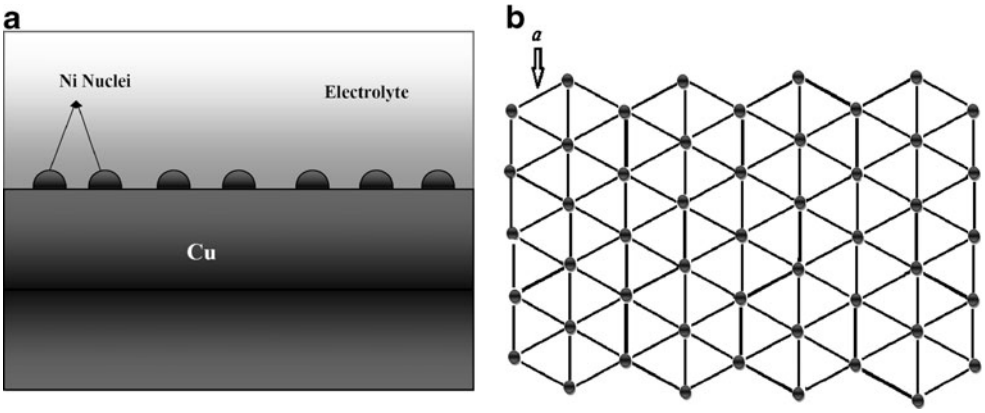

Fig. 5 Sketches of the optical model used for the simulation of instantaneous Ni nucleation: **a** hemispherical Ni nuclei form on the Cu substrate, **b** they are arranged in a hexagonal array with a distance *a* between nucleation centres

the electrochemical nucleation of metals on extraneous substrates lie in the range 10^4–10^{10} cm^{-2} [35]. On the basis of these figures, a reasonable value of the thickness of the nucleation layer to be used in our simulations can be taken to be 100 nm. Assuming that the number density of nuclei is constant, the relationship between the radius of the nuclei r_N and the volume fraction f_1 of Ni in the MG model is:

$$f_1 = \frac{32\pi}{9\sqrt{3}} \cdot \left(\frac{r_N}{a}\right)^3 \tag{6}$$

(i.e. $f_1 = \frac{4\pi}{9\sqrt{3}} \cong 0.81$ corresponds to a hexagonal compact monolayer of nuclei with $r_N = \frac{a}{2}$).

The computed reflectivity $R(f_1)$ for this Ni nucleation model is shown in Fig. 6a. It can be observed that by increasing the volume fraction f_1 of Ni, initially the $R(f_1)$ value of reflectivity decreases. As the Ni volume fraction increases, an increase in reflectivity is obtained. By comparing $R(f_1)$ with the normalised experimental $R(V)$ for the interval −0.90 to −1.45 V (region II, the full experimental curve is reported in Fig. 4a): a reasonable qualitative agreement is found, supporting our interpretation of the relevant R transient in terms of nucleation. The measured thickness of deposits obtained under identical conditions by stopping the LSV at −1.0 and −1.3 V, were found to be 7±2 and 52±4 nm, respectively: these values are in reasonable agreement with the estimates of 3 and 79 nm derived from the geometrical model adopted for the interpretation of the reflectivity data.

The decrease of reflectivity in region III of Fig. 4a can be explained by the thickening and roughening of the Ni film during the 3D growth period. Reflectivity simulations as a function of thickness for a selection of roughness values are reported in Fig. 6b: it can be noticed that an increase in thickness gives rise to an increase of R, but an increase in roughness causes a decrease of R. The film obtained by stopping the LSV at −1.8 V exhibits a thickness of 142±7 nm and an AAR of 57 nm. The reflectivity value related to this potential derived from the experimental reflectivity transient (Fig. 4a) is 0.31: this experimental point is shown by a red pentagon overlapped to the plot showing the

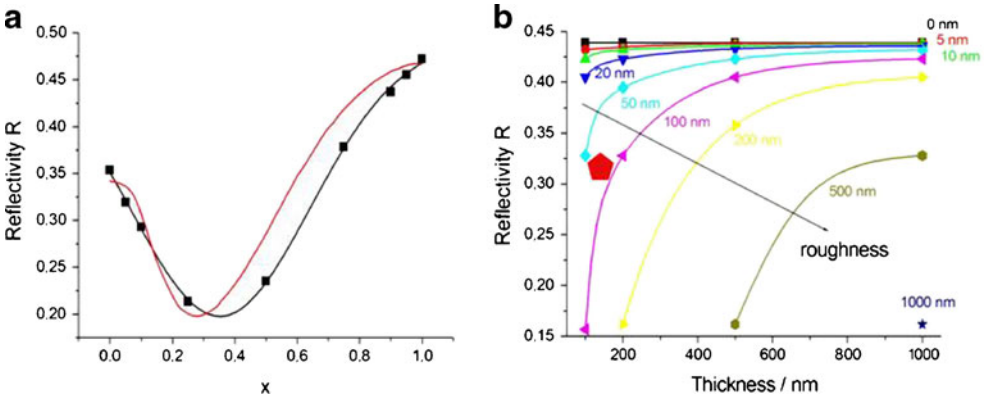

Fig. 6 Nickel electrodeposition. **a** Comparison of experimental Ni reflectivity transient (*red line*; data from Fig. 4a, region II) and simulated reflectivity derived from a Ni nucleation model (*squares* are computed points, the *black line* is a guide for the eye): normalised experimental data, *x* axis corresponds to f_1 for the computed R (*black points and curve*) and the applied potential is $[(1-x)\cdot 0.55-1.45]$ V to the normalised potential interval of region II, Fig. 4a for the experimental R (*red curve*). **b** Simulated reflectivity for a 3D Ni film as a function of thickness and roughness. The *red pentagon* represents an experimental point. The *lines* are a guide for the eye

computed reflectivity curves (Fig. 6b) demonstrating a sound quantitative agreement.

SEM micrographs of three samples prepared by stopping the LSV at the end potentials: −1.0, −1.3, and −1.8 V, corresponding to critical points of both reflectivity and current density transients, are shown in Fig. 7: it can be observed that smooth, crack-free layers, not exhibiting unstable growth features on the length scale typical for electrodeposition studies, were obtained at these three potentials; these morphologies are coherent with the model used for the interpretation of the reflectivity transients.

Reflectivity transient recorded during electrodeposition from the Ni/low-cerium solution

The reflectivity and LSV curves measured with the Ni solution containing a low Ce(III) concentration are shown in Fig. 4b. The reflectivity transient can be divided into five regions. In region I, upon decreasing the potential from −0.3 to −0.9 V, the values of reflectivity and current density are approximately constant. In region II, decreasing the potential below −0.9 V a drop in the reflectivity is obtained, followed by a small increase until a maximum is reached at ca. −1.1 V; in this region, the current density also drops monotonically up to ca. −1.3 V. Upon decreasing the potential to values lower than −1.1 V (region III), a second sharp drop in reflectivity is recorded, followed by an increase, characterised by a change of slope at ca. −1.3 V (regions III and IV). In region IV, going cathodic in the potential interval of −1.3 to −1.7 V increases reflectivity at a rate lower than in region III. At still lower potentials (region V), the reflectivity exhibits a slight decrease.

The reflectivity transient of region II, containing a decrease, followed by a maximum (before a second decreasing interval—in region III—that will be commented below), can be discussed is terms of Ni nucleation on the Cu substrate, along the same lines proposed in "Reflectivity transient recorded during nickel electrodeposition" section. The simulation of this first nucleation process, together with the experimental reflectivity transient of region II, is shown in Fig. 8a: from the comparison of the experimental and computed curves, it can be concluded that after this first nucleation process, only ca. 40 % of the Cu surface is covered by Ni nuclei. A possible explanation of this fact could be that—owing to the pH drift in the catholyte accompanying the electrodeposition process—the rest of the Cu surface is covered with cerium hydroxide: this interpretation is coherent with the cathodic passivation observed in the corresponding current density curve (Fig. 4b).

In principle, the second drop of reflectivity in region III can result from two possibly concurrent processes: embedding of cerium oxide/hydroxide and secondary nucleation of Ni (i.e. the surface of the previously grown first Ni/cerium hydroxide composite film becomes covered with a new layer of Ni nuclei); it is worth noting that secondary nucleation processes have been described in the literature [36]. In

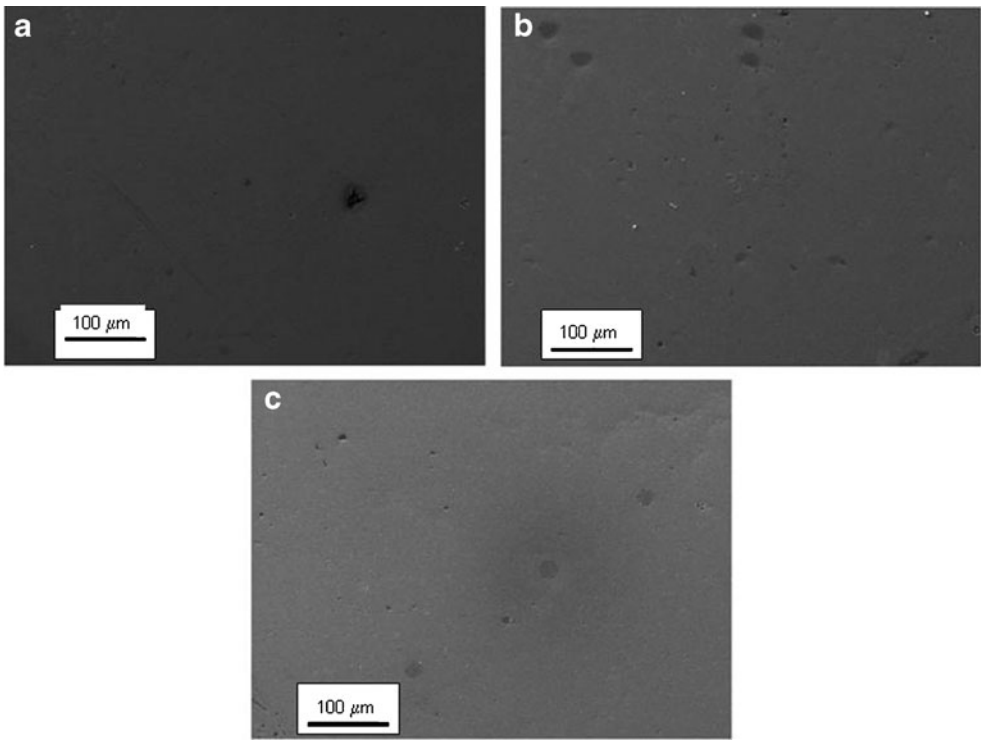

Fig. 7 SEM images of Ni films prepared by stopping the linear potential sweep at the following end potentials: **a** −1.0, **b** −1.3, and **c** −1.8 V vs. Ag/AgCl

order to assess quantitatively the corresponding optical effects, cerium oxide embedding into the Ni-containing electrodeposit, was simulated with the model described in "Spectroscopic ellipsometry measurements and modelling" section. The results of our computations, not reported here for brevity, unambiguously show that embedding of cerium in the Ni layer cannot explain the observed decrease in reflectivity. The simulation of secondary nucleation of Ni is reported in Fig. 8b, together with the experimental reflectivity transient of region III: a sound qualitative matching of the computed and measured quantities was found. By comparing the simulation and experimental test, it can be observed that at the end of the secondary nucleation process, only ca. 25 % of the first layer is covered by secondary Ni nuclei. For the same reasons given in the discussion of region II, we can consider that the rest of the cathode surface is covered with cerium hydroxide. In order to further validate our model, we grew films by stopping the LSV at −1.0 and −1.3 V and measured the corresponding film thicknesses that resulted to be 6±1 and 61±3 nm, respectively; in good agreement with the corresponding estimates of 3.2 and 100 nm obtained from the optical model.

For potentials in the interval ca. −1.3 to −1.65 V (region IV of Fig. 4b), the reflectivity still increases, but with a lower slope. Eventually, in the interval ca. −1.65 to −1.80 V (region V of Fig. 4b), it reaches an asymptotic value. Such increase can be explained with the thickening of a Ni/cerium oxide film with a low content of the dispersoid. In order to rationalise this explanation, we have modelled the dependence of reflectivity on the amount of cerium oxide (the details are omitted for brevity); coherently with the observed morphology (see Fig. 9a and background of Fig. 9b–d) and in order to reduce the model parameters, we considered ideally smooth films. The best comparison with experimental results was found with 7 % ceramic phase (Fig. 8c). The experimental and computed data are in sound qualitative agreement. The slight decrease in reflectivity observed in region V can be explained—as in the previous section (see Fig. 6b and corresponding discussion)—with the surface roughening accompanying 3D growth. Reflectivity simulations as a function of thickness for a selection of roughness values are reported in Fig. 8d: as commented above referring to Fig. 6b, it can be noticed that an increase in thickness gives rise to an increase of R, but an increase of roughness causes a decrease in R. The coating obtained by stopping the LSV at −1.8 V exhibits a thickness of 95±4 nm and an AAR of 17±4 nm. The reflectivity value related to this potential derived from experimental reflectivity transient (Fig. 4b) is 0.168: this experimental point is shown by a red pentagon together with the computed reflectivity curves in Fig. 8d, showing a sound quantitative agreement.

With the same approach adopted in "Reflectivity transient recorded during nickel electrodeposition" section, we grew three samples with the same electrical parameters, from the Ni/low-cerium electrodeposition bath. Figure 9 reports SEM images of these samples. One can observe that a smooth and crack-free coating was obtained at −1.0 V (a), while at −1.3 V (b), secondary nucleation can be observed. Panels c and d, referring to −1.8 V, show a progressive increase in the number density of nuclei. Micrography thus supports the explanation that the second drop in reflectivity is related to secondary nucleation. A schematic overview of the secondary nucleation process is depicted in Fig. 10: after completion of the primary nucleation step (panel a); owing to the alkalinisation of the catholyte, cerium hydroxide forms (panel b); and secondary nucleation occurs on the previously grown Ni/cerium hydroxide composite layer (panel c).

Reflectivity transient recorded during electrodeposition from the Ni/high-cerium solution

The reflectivity and LSV curves measured with the Ni solution containing a high Ce(III) concentration are shown in Fig. 4c. The reflectivity curve can be divided into three regions, as shown in the plot. Two successive drops in reflectivity are observed in the regions II and III, with two changes in slope at ca. −1.0 and −1.2 V. The fist fall in the curve (region II) can again be explained with Ni nucleation as in the sections on "Reflectivity transient recorded during nickel electrodeposition" and "Reflectivity transient recorded during electrodeposition from the Ni/low-cerium solution". As far as the current density is concerned, a cathodic passivation peak is observed in the interval ca. −1.0 to −1.3 V, for more cathodic polarisations, a conventional Tafel-type behaviour is found. According to the model proposed in the "Reflectivity transient recorded during electrodeposition from the Ni/low-cerium solution" section, also this behaviour can be rationalised in terms of secondary nucleation and growth of a rough layer of hydrous cerium oxide. In this particular system, the growth process ensuing secondary nucleation causes a sharp decrease in the value of reflectivity, at variance with what we found with the low-cerium bath. This phenomenology can be related to the results of previous studies [37], highlighting that the formation of cerium-rich films acts as a barrier tending to stop the Ni electrodeposition process.

The simulation of the first nucleation, together with the experimental reflectivity transient corresponding to region II, is shown in Fig. 11a. The simulated reflectivity curve is in qualitative agreement with the measured one and the results allow to estimate that after this first nucleation process, only ca. 30 % of the cathode surface is covered by Ni nuclei. Figure 11b shows the result of reflectivity simulations for a film of hydrated cerium oxide as a function of thickness and roughness. The red stars shown in the plot are

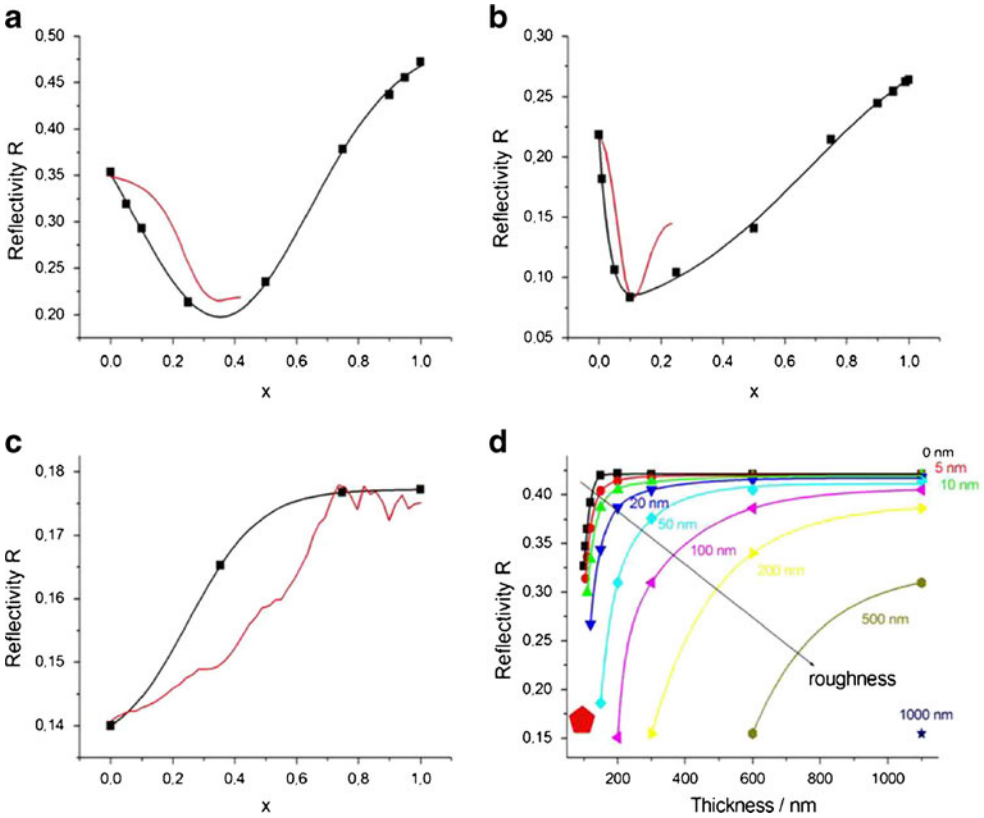

Fig. 8 Ni/cerium oxide electrodeposition from a low-cerium solution. **a**–**c** Comparisons of experimental Ni reflectivity transient (*red lines* data from Fig. 4b: **a** region II, **b** region III, **c** regions IV and V) and simulated reflectivity derived from a Ni nucleation model (*squares* computed points, *black line* guide for the eye): normalised experimental data, *x* axes correspond to: **a** f_1 for the computed *R* and [−0.9−0.5·*x*] *V* for the applied potential; **b** f_1 for the computed *R* and [−1.1−0.83·*x*] V for the applied potential, **c** thickness [*x*·110] nm for the computed *R* and [−1.3−0.5·*x*] *V* for the applied potential. **d** Simulated reflectivity for a 3D Ni/cerium oxide (7 %) film as a function of thickness and roughness. The *red pentagon* represents an experimental point. The *lines* are a guide for the eye

experimental values obtained by preparing films by stopping the LSV at −1.3 and −1.8 V: the measured thicknesses were respectively 69±6 and 73±5 nm, their roughness 2.6±1.5 and 9.0±2.8 nm and their reflectivities 0.22 and 0.15. In order to assess the potential-dependent morphology of the composite films, with the same approach as in the two previous sections, we have electrodeposited three samples by scanning the potential from −0.3 V to cathodic terminal

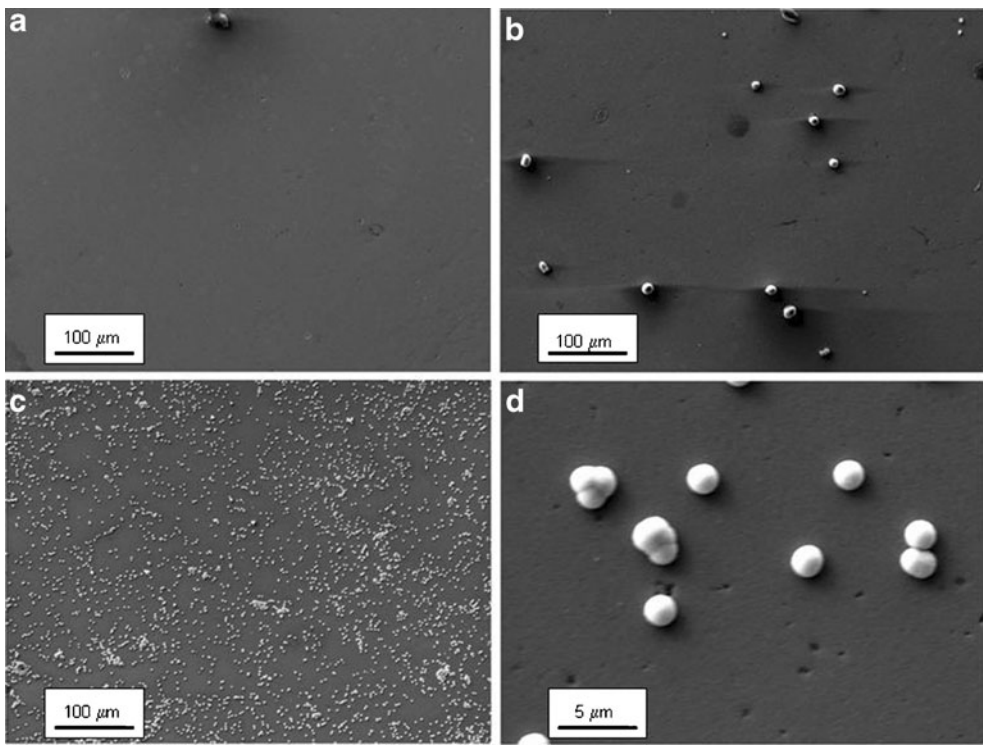

Fig. 9 SEM images of Ni/low-cerium oxide films prepared by stopping the linear potential sweep at the following end potentials **a** −1.0, **b** −1.3, **c**, **d** −1.8 V vs. Ag/AgCl

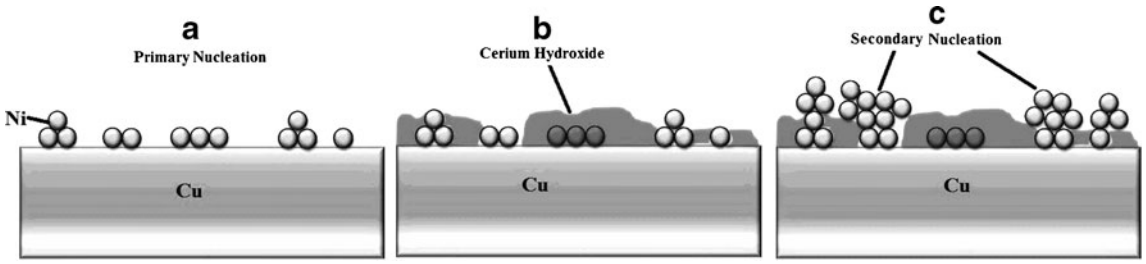

Fig. 10 Schematic view of the secondary nucleation process **a** primary nucleation of Ni, **b** precipitation of cerium hydroxide, and **c** secondary nucleation of Ni

voltages of −1.0, −1.3 and −1.8 V and examined the surfaces by SEM (Fig. 12). It can be noticed that the coating obtained at −1.0 V is smooth and crack free; at −1.3 V, only traces of secondary nucleation can be detected, while at −1.8 V, secondary nucleation is obvious. The reason why secondary nucleation is shifted to polarisations more cathodic than −1.3 V in the bath containing a high concentration of Ce(III) is probably related to this fact that cerium hydrous oxide tends to cover the entire surface, so that secondary nucleation of Ni requires a higher crystallisation overvoltage and is favoured in correspondence of cracks or defects [38], as highlighted in Fig. 12e. A higher magnification micrograph of the film grown at −1.8 V, recorded with backscattered electrons outside the secondary nucleation area, is shown in Fig. 12d: cerium hydrous oxide particles can be identified from the white aspect resulting from compositional contrast.

In situ surface Raman spectroscopy and X-ray photoelectron spectroscopy

In order to obtain molecular information on the dynamic electrodeposition interface, we measured Raman spectra in situ during electrodeposition from the Ni solutions containing 0 (pure Ni), 1 mM (Ni/low-cerium oxide) and 5 mM (Ni/high-cerium oxide) $CeCl_3.7H_2O$: our results are reported in Fig. 13. At OCP, two bands are present at 877 and 1,599 cm^{-1}, corresponding to $B(OH)_3$ stretching (876 cm^{-1}) [39] and NiOOH bending (1,600 cm^{-1}) [40]: the band related to boric acid is visible under all the investigated conditions. At −1.0 V both the Ni and Ni/low-cerium baths exhibit two new broad bands at ca. 475 and 750 cm^{-1}: similar surface Raman bands were observed in [41] and assigned to ν(NiO) and δ(NiOH). It is worth noting that the pure-Ni and low-cerium baths exhibit a very similar spectral behaviour. The high cerium bath exhibits a different behaviour: a new broad band at 1,260 cm^{-1} is the only feature present at −1.0 V: this new band can be assigned to defected CeO_2 fluorite structure [42, 43]. It is worth recalling that in this system, full coverage with cerium-containing basic salts was found to take place at low cathodic polarisations (see "Reflectivity transient recorded during electrodeposition from the Ni/high-cerium solution" section). As the potential is shifted to −1.3 V, the intensity of the band at 1,260 cm^{-1} decreases, and that of the band at

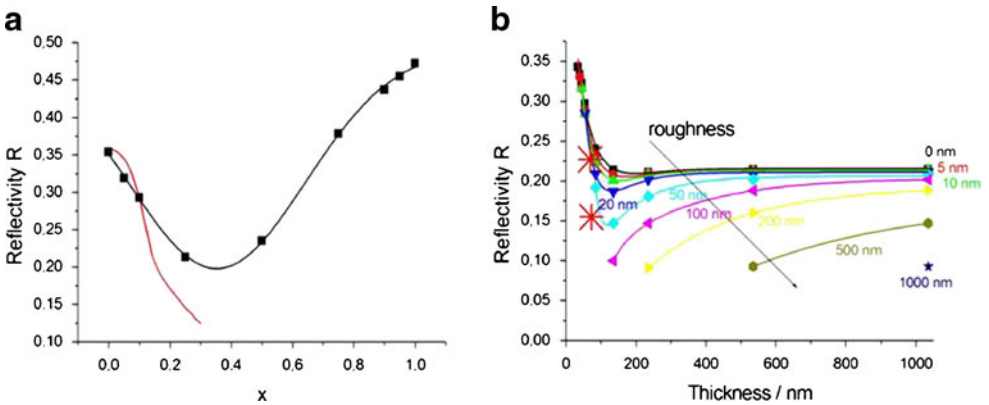

Fig. 11 Ni/cerium oxide electrodeposition from a high-cerium solution. **a** Comparison of experimental reflectivity transient (*red line* data corresponding to Fig. 4c, region II) and simulated reflectivity (*squares* computed points, *black line* guide for the eye): normalised experimental data, x axis corresponds to: f_1 for the computed R and $[-0.9-0.2{\cdot}x]$ V for the applied potential. **b** Simulated reflectivity for Ni nucleation as a function of thickness and roughness. The *red stars* represent experimental points. The *lines* are a guide for the eye

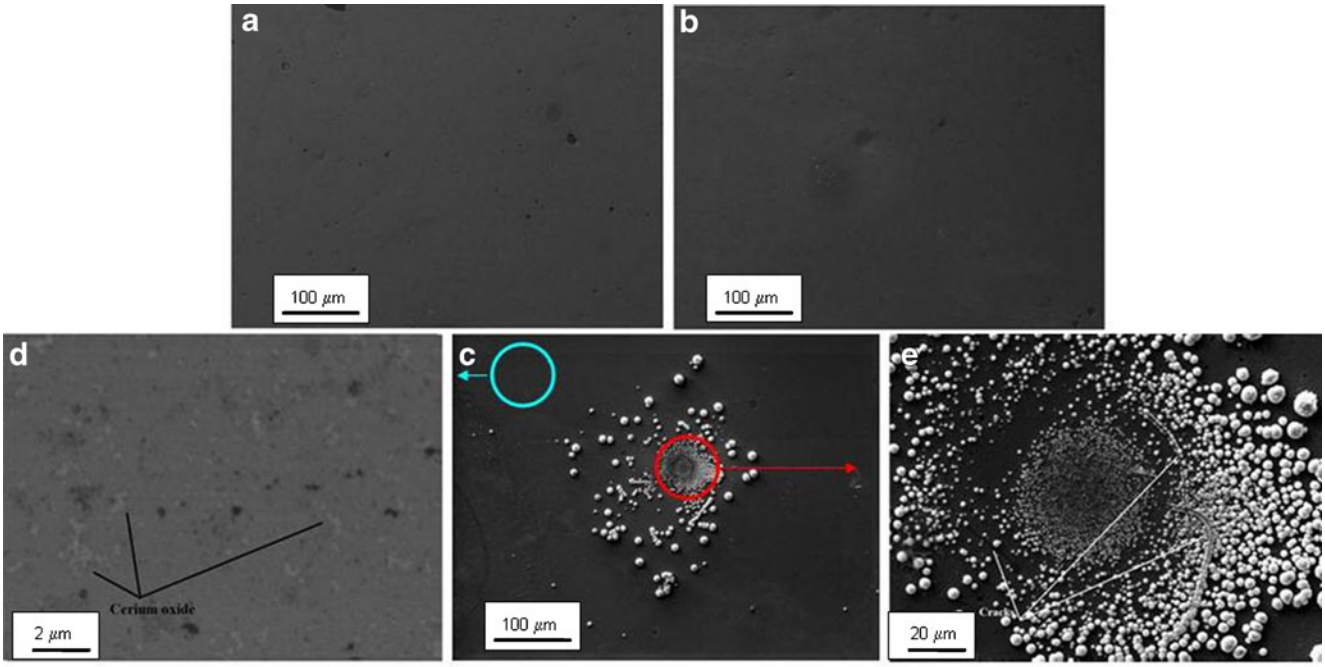

Fig. 12 SEM images of Ni/high-cerium oxide film prepared by stopping the linear potential sweep at different end potentials **a** −1.0 V, **b** −1.3 V, **c** −1.8 V vs. Ag/AgCl. **d** 3D magnifications of the indicated areas of **c**

475 cm^{-1}, characteristic of NiOH, increases, coherently with the fact that Ni renucleates on the cerium oxide rich surface that had formed at −1.0 V.

Figure 14 depicts the Ce 3d region of high-resolution XPS spectra obtained with cerium oxide in the Ni-matrix composite coating. Peak deconvolution yields six peaks, whose energies are typical for Ce(IV) and Ce(III). We can thus conclude that Ce is present in our films in the form of mixed, nonstoichiometric oxides with a Ce(IV)/Ce(III) ration of 1.17 [44].

Conclusions

In the present paper, we have studied the electrodeposition of Ni/Ce-oxide composites from a single bath containing nickel and cerium salts: the investigation is based on in situ spectroelectrochemical methods—visible electroreflectance and Raman—able to disclose subtle compositional and molecular details of the dynamic interface during electrochemical growth. The reflectivity curves measured with the pure

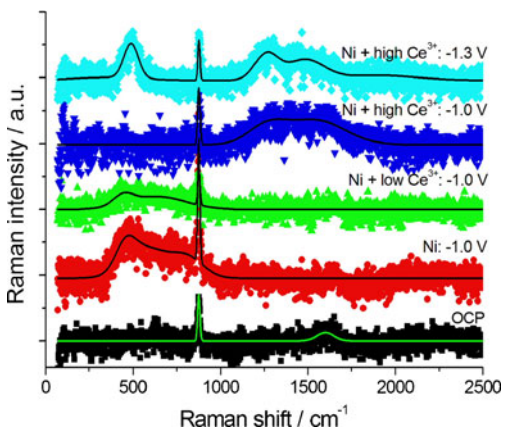

Fig. 13 In situ Raman spectra measured in situ during electrodeposition at the indicated potentials from following solution solutions: pure Ni, Ni/low-cerium oxide and Ni/high-cerium oxide

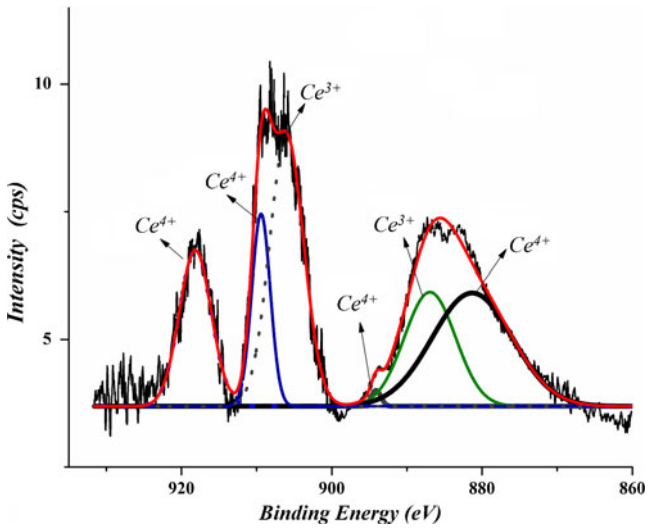

Fig. 14 High-resolution X-ray photoelectron spectra (XPS) of the Ce 3D region for Ni-cerium oxide film deposited on Cu after 1 min Ar^{+} etching

Ni and cerium-containing solution sharply drops when the potential is less than ca. −0.9 V. For cathodic polarisations exceeding −1.1 V, in the pure Ni bath the reflectivity grows again, while in the presence of Ce^{3+}, it shows another decrease. On the basis of numerical simulations of the optical properties of the electrochemical interface, the initial reflectivity drop can be explained in terms of Ni nucleation on the Cu substrate. The second reflectivity drop observed with the cerium-containing solutions is instead due to secondary nucleation of Ni. Our results suggest that the Ni deposition process can be divided into two steps: (1) nuclation and (2) 3D growth, accompanied by roughening. The codeposition process of Ni/cerium oxide goes on through four stages: (1) primary nucleation of Ni onto the Cu cathode, (2) formation of a cerium oxide film, (3) secondary nucleation of Ni, and (4) 3D growth and roughening of the composite film.

Acknowledgments Assistance in laboratory activities is gratefully acknowledged to Elisabetta Tondo and Francesco Bogani, Dipartimento di Ingegneria dell'Innovazione, Università del Salento, Italy.

References

1. Xue YJ, Jia XZ, Zhou YW, Ma W, Li JS (2006) Tribological performance of Ni–CeO_2 composite coatings by electrodeposition. Surf Coat Technol 200:5677–5681
2. Qu NS, Zhu D, Chan KC (2006) Fabrication of Ni–CeO_2 nanocomposite by electrodeposition. Scripta Mater 54:1421–1425
3. Zhitomirsky I (2002) Cathodic electrodeposition of ceramic and organoceramic materials. Fundamental aspects. Adv Colloid Interface Sci 97:279–317
4. Zhou Y, Switzer JA (1996) Growth of cerium(IV) oxide films by the electrochemical generation of base method. J Alloys Compd 237:1–5
5. Zhitomirsky I, Petric A (2001) Electrochemical deposition of ceria and doped ceria films. Ceram Int 27:149–155
6. Qi Wang A, Golden TD (2003) Anodic electrodeposition of cerium oxide thin films. J Electrochem Soc 150:616–620
7. Golden TD, Qi Wang A (2003) Anodic electrodeposition of cerium oxide thin films II. Mechanism studies. J Electrochem Soc 150: C621–C624
8. Hamlaoui Y, Pedraza F, Remazeilles C, Cohendoz S, Rébéré C, Tifouti L, Creus J (2009) Electrodeposition of cerium-based oxides on carbon steel from concentrated cerium nitrate solutions. Part I. Electrochemical and analytical characterization. Mater Chem Phys 113:650–657
9. Yang L, Pang X, Fox-Rabinovich G, Veldhuis S, Zhitomirsky I (2011) Electrodeposition of cerium oxide films and composites. Surf Coat Technol 206:1–7
10. Hayes SA, Yu P, O'Keefe TJ, O'Keefe MJ, Stoffer JO (2002) The phase stability of cerium species in aqueous systems I. E-pH diagram for the Ce-HClO4-H2O system. J Electrochem Soc 149:623–630
11. Tondo E, Boniardi M, Cannoletta D, D'Elia M, D'Urzo L, Bozzini B (2009) Electrodeposition of NiO/YSZ from hydroalcoholic solutions containing chitosan. Surf Coat Technol 203:3427–3434
12. Tondo E, Boniardi M, Cannoletta D, De Riccardis MF, Bozzini B (2010) Electrodeposition of yttria/cobalt-oxide and yttria/gold coatings onto ferritic stainless steel for SOFC interconnects. J Power Sourc 195:4772–4778
13. Bozzini B, Tondo E, Raffa P, Boniardi M (2012) Electrodeposition of Y2O3-Au composite coatings for SOFC interconnects: in situ monitoring of film growth by surface-enhanced Raman spectroscopy. Trans Inst Met Finish 90:30–37
14. Li J, Xiong D, Huang Z, Kong J, Dai J (2009) Effect of Ag and CeO2 on friction and wear properties of Ni-base composite at high temperature. Wear 267:576–584
15. Zhang Z, Lu X, Han B, Luo J (2007) Rare earth effect on the microstructure and wear resistance of Ni-based coatings. Mater Sci Eng, A 454–455:194–202
16. Han B, Lu X (2008) Tribological and anti-corrosion properties of Ni–W–CeO2, coatings against molten glass. Surf Coat Technol 202:3251–3256
17. Yang W, Chu W, Jiang C, Wen J, Sun W (2011) Cerium oxide promoted Ni/MgO catalyst for the synthesis of multi-walled carbon nanotubes. Chin J Catal 32:1323–1328
18. Tang LP, Diamond L, Macdonald M, Mcmillan BG, Morrow J, Spicer MD, Berlouis LEA, Weston M (2009) Impact of synthesis temperature on hydrogen storage and emission from Ni/Ce composite oxides. Int J Hydrogen Energ 34:7296
19. Tang LP, Diamond L, MacDonald M, McMillan BG, Morrow J, Spicer MD, Berlouis LEA, Weston M (2009) Impact of synthesis temperature on hydrogen storage and emission from Ni/Ce composite oxides. Int J Hydrogen Energ 34:7296–7305
20. Li Y, Fu Q, Flytzani-Stephanopoulos M (2000) Low-temperature water–gas shift reaction over Cu- and Ni-loaded cerium oxide catalysts. Appl Catal, B 27:179–191
21. Hasannejad H, Shahrabi T, Jafarian M, Rouhaghdam AS (2011) EIS study of nano crystalline Ni-cerium oxide coating electrodeposition mechanism. J Alloys Compd 509:1924–1930
22. Bozzini B, D'Urzo L, Mele C (2005) Electrodeposition of Cu from cyanoalkaline solutions in the presence of CPC and PEG. J Electrochem Soc 152:C255–C264
23. Bozzini B, Mele C, D'Urzo L, Giovannelli G, Natali s (2006) Electrodeposition of Cu from acidic sulphate solutions in the presence of PEG: an electrochemical and spectroelectrochemical investigation–part I. J Appl Electrochem 36:789–800
24. Bozzini B, Gianoncelli A, Kaulich B, Kiskinova M, Prasciolu M, Sgura I (2010) Metallic plate corrosion and uptake of corrosion products by nafion in polymer electrolyte membrane fuel cells. Chem Sus Chem 7:846–850
25. Bozzini B, Gianoncelli A, Kaulich B, Kiskinova M, Mele C, Prasciolu M (2011) Corrosion of Ni in 1-butyl-1-methyl-pyrrolidinium bis (trifluoromethylsulfonyl) amide room-temperature ionic liquid: an in-situ X-ray imaging and spectromicroscopy study. Phis Chem Chem Phys 13:7968–7974
26. Bozzini B, Tondo E, Amati M, Kazemian M, Gregoratti L, Kiskinova M (2011) In-situ X-ray spectromicroscopy investigation of the material stability of SOFC metal interconnects in operating electrochemical cell. Chem Sus Chem 4:1099–1103
27. Bozzini B, D'Urzo L, Mele C, Romanello V (2008) A SERS investigation of cyanide adsorption and reactivity during the electrodeposition of gold, silver, and copper from aqueous cyanocomplex solutions. J Phys Chem C, Nanomater Interface 112:6352–6358
28. Bozzini B, D'Urzo L, Mele C (2007) A novel polymeric leveller for the electrodeposition of copper from acidic sulphate bath: a spectroelectrochemical investigation. Electrochim Acta 52:4767–4777
29. Tondo E, Mele C, Bozzini B (2010) Silver electrodeposition from water-acetonitrile mixed solvents. Part III—an in situ investigation by optical second harmonic generation spectroscopy. J Solid State Electrochem 14:989–995
30. Sgura I, Bozzini B (2005) Numerical issues related to the modelling of electrochemical impedance data by non-linear least-squares. Int J Non lin Mech 40:557–570
31. Bozzini B, Sgura I (2008) A class of mathematical models for alternated-current electrochemical measurements accounting

for non-linear effects. Nonlinear Anal R World Appl 9:412–429
32. Bozzini B, Mele C, D'Urzo L (2006) Electrodeposition of Cu from acidic sulphate solutions in the presence of PEG—part II visible electroreflectance spectroscopy measurements during electrodeposition. J Appl Electrochem 36:87–96
33. Bozzini B, D'Urzo L, Mele C (2008) Electrochemical fabrication of nano- and micrometric Cu particles: in situ investigation by electroreflectance and optical second harmonic generation. Trans Inst Met Fin 86:267–274
34. Li W, Zhang S (2011) In situ ellipsometric study of electrodeposition of manganese films on copper. Appl Surf Sci 257:3275–3280
35. Ispas A, Matsushima H, Bund A, Bozzini B (2009) Nucleation and growth of thin nickel layers under the influence of a magnetic field. J Electroanal Chem 626:174–182
36. Orinakova R, Streckova M, Trnkova L, Rozik R, Galova M (2006) Comparison of chloride and sulphate electrolytes in nickel electrodeposition on a paraffin impregnated graphite electrode. J Electroanal Chem 594:152–159
37. Sorkhabi HA, Haghighi MM, Hosseini MG (2008) Effect of rare earth (Ce, La) compounds in the electroless bath on the plating rate, bath stability and microstructure of the nickel–phosphorus deposits. Surf Coat Technol 202:1615–1620
38. Chang HK, Choe B-H, Lee JK (2005) Influence of titanium oxide films on copper nucleation during electrodeposition. Mater Sci Eng, A 409:317–328
39. Xiaoping L, Shiyang G, Shuping X (2004) Investigations of kinetics and mechanism of chloropinnoite in boric acid aqueous solution at 303 K by Raman spectroscopy. Spectrochim Acta Part A 60:2725–2728
40. De Riccardis MF, Carbone D, Martina V, Re M, Bozzini B, D'Urzo L (2009) Study on the adhesion mechanism of electrodeposited nickel clusters on carbon Substrates. Appl Surf Sci 255:4309–4315
41. Deabate S, Fourgeot F, Henn F (2000) X-ray diffraction and micro-Raman spectroscopy analysis of new nickel hydroxide obtained by electrodialysis. J Power Sourc 87:125–136
42. Shan WJ, Feng ZC, Li ZL, Jing Z, Shen WJ, Can L (2004) Oxidative steam reforming of methanol on $Ce_{0.9}Cu_{0.1}O_Y$ catalysts prepared by deposition—precipitation, coprecipitation, and complexation—combustion methods. J Catal 228:206–217
43. Ferreira AC, Ferraria AM, Botelho do Rego AM, Goncalves AP, Girão V, Correia R, Almeida Gasche T, Branco JB (2010) Partial oxidation of methane over bimetallic copper—cerium oxide catalysts. J Mol Catal Chem 320:47–55
44. Wang KL, Zhang QB, Sun ML, Wei XG, Zhu YM (2001) Appl Surf Sci 174:191